



## Research article

# Magnetic ordering in GdAuAl<sub>4</sub>Ge<sub>2</sub> and TbAuAl<sub>4</sub>Ge<sub>2</sub>: Layered compounds with triangular lanthanide nets

Keke Feng<sup>a,b</sup>, Ian Andreas Leahy<sup>b</sup>, Olatunde Oladehin<sup>a,b</sup>, Kaya Wei<sup>b</sup>, Minhyea Lee<sup>c</sup>, Ryan Baumbach<sup>a,b,\*</sup>

<sup>a</sup> Department of Physics, Florida State University, United States of America

<sup>b</sup> National High Magnetic Field Laboratory, United States of America

<sup>c</sup> Department of Physics, University of Colorado Boulder, United States of America

## ARTICLE INFO

## Keywords:

Centrosymmetric compounds  
Magnetic frustration

## ABSTRACT

We report the synthesis and magnetic properties of GdAuAl<sub>4</sub>Ge<sub>2</sub> and TbAuAl<sub>4</sub>Ge<sub>2</sub>, where temperature and magnetic field dependent magnetization, heat capacity, and electrical resistivity measurements reveal that both compounds exhibit several magnetically ordered states at low temperatures, with evidence for magnetic fluctuations extending into the paramagnetic temperature region. For magnetic fields applied in the *ab*-plane there is particularly rich behavior, with several ordered state regions that are separated by metamagnetic phase transitions. Despite Gd being an isotropic *S*-state ion and Tb having an anisotropic *J*-state, there are similarities in the phase diagrams for the two compounds, suggesting that factors such as the symmetry of the crystalline lattice, which features well separated triangular planes of lanthanide ions, or the Ruderman–Kittel–Kasuya–Yosida interaction control the magnetism. We also point out similarities to other centrosymmetric compounds that host skyrmion lattices such as Gd<sub>2</sub>PdSi<sub>3</sub>, and propose that the *Ln*AuAl<sub>4</sub>Ge<sub>2</sub> family of compounds are of interest as reservoirs for complex magnetism and electronic behaviors.

## 1. Introduction

Intermetallic *f*-electron materials have attracted sustained interest for decades because they are hosts for a variety of interesting phenomena. This includes complex local moment order [1,2], ferromagnetic states with industrial applications [3,4], heavy fermion behavior [5], emergent ordered states [6,7], unconventional superconductivity [8], and nontrivial electronic and magnetic topologies [9]. These states occur due to a complex interplay between the lattice, charge, orbital, and spin degrees of freedom, through channels such as the Ruderman–Kittel–Kasuya–Yosida (RKKY) interaction [10–12], crystal electric field splitting [13] and the Kondo interaction [14]. Very recently, there has been a surge of interest in a new group of lanthanide intermetallics, namely centrosymmetric metals that exhibit skyrmion states in the absence of a Dzyaloshinskii–Moriya (DM) interaction [15–20]. This is contrasted with earlier studies of materials such as MnSi [21] and Fe<sub>0.5</sub>Co<sub>0.5</sub>Ge [22], where the non-centrosymmetric crystal structure produces the DM interaction. In this new group of materials, a delicate balance between the crystalline anisotropy and various magnetic energy scales (e.g., geometric frustration [23,24], competing RKKY interactions [25–27]), and possibly crystal electric field effects [28–30]

combine to produce their complex magnetic states. However, it is still unclear how to design new examples with enhanced properties.

Motivated by this, we recently investigated the weakly correlated *f*-electron metal CeAuAl<sub>4</sub>Ge<sub>2</sub> [31,32], where the planar triangular arrangement of the cerium ions resembles what is seen for Gd<sub>2</sub>PdSi<sub>3</sub> [19, 33]. In this case, we demonstrated that the cerium ions are trivalent, are weakly interacting, and there is limited evidence for magnetic frustration. This led us to consider the effect of strengthened magnetic interactions: e.g., by replacing Ce with other lanthanides (*Ln*) ions. Here we report the synthesis of single crystals of the entire *Ln*AuAl<sub>4</sub>Ge<sub>2</sub> series and focus on the magnetic properties of GdAuAl<sub>4</sub>Ge<sub>2</sub> and TbAuAl<sub>4</sub>Ge<sub>2</sub>. These examples not only are expected to have large effective magnetic moments ( $\mu_{\text{eff}} = 7.94 \mu_{\text{B}}/\text{Gd}$  and  $9.72 \mu_{\text{B}}/\text{Tb}$ ), but also allow a comparison between a pure spin ion (Gd<sup>3+</sup>;  $S = 7/2$ ,  $L = 0$ ,  $J = 7/2$ ) and a mixed spin–orbital ion (Tb<sup>3+</sup>;  $S = 3$ ,  $L = 3$ ,  $J = 6$ ). Temperature and field dependent magnetization measurements reveal that GdAuAl<sub>4</sub>Ge<sub>2</sub> shows little anisotropy in the paramagnetic state while TbAuAl<sub>4</sub>Ge<sub>2</sub> shows easy *ab*-plane anisotropy. Complex magnetic ordering appears at low temperatures for both compounds, where GdAuAl<sub>4</sub>Ge<sub>2</sub> has three magnetic phase transitions at  $T_{\text{N1}} = 17.8 \text{ K}$ ,  $T_{\text{N2}} =$

\* Corresponding author at: National High Magnetic Field Laboratory, United States of America.  
E-mail address: [baumbach@magnet.fsu.edu](mailto:baumbach@magnet.fsu.edu) (R. Baumbach).

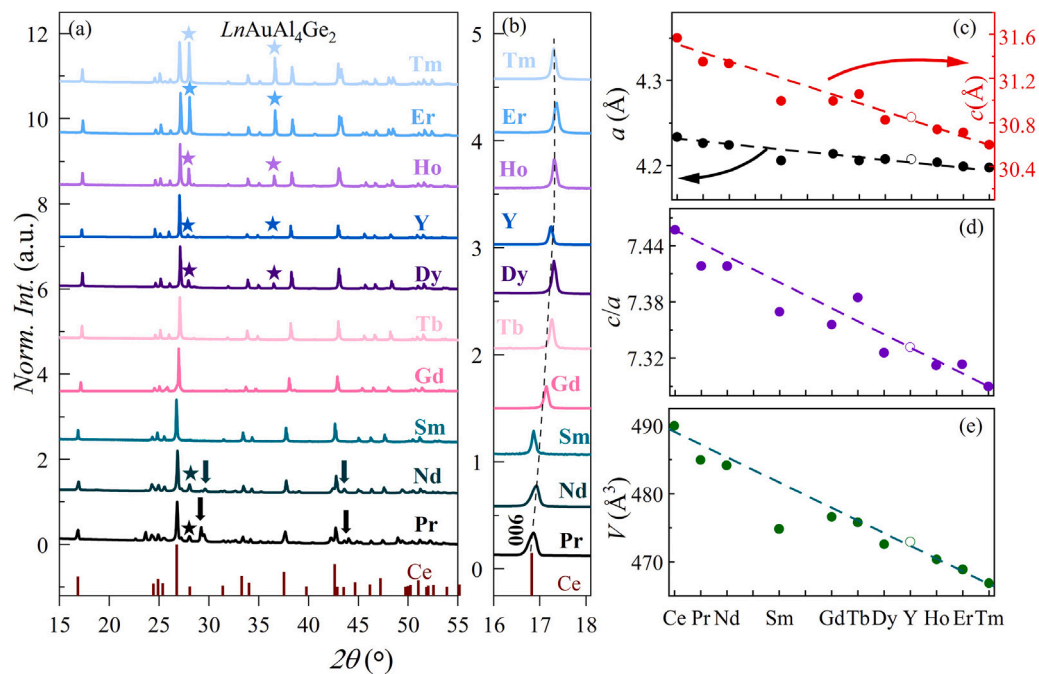


**Fig. 1.** (a) Powder X-ray diffraction data for  $LnAuAl_4Ge_2$  ( $Ln = Y, Pr, Nd, Gd, Tb, Dy, Ho, Er,$  and  $Tm$ ). The normalized intensity patterns are compared to the theoretical peaks for  $CeAuAl_4Ge_2$  [31] and have been shifted vertically for clarity. The impurity peaks associated with  $LnAl_2Ge_2$  and  $AuAl_2$  are marked with stars and arrows, respectively. (b)  $Ln$  dependence of the diffraction peak at 006. The dashed line is a guide to the eye. (c) The lattice constants  $a$  and  $c$  were determined from Rietveld analysis of powder X-ray diffraction measurements. Results for Ce are from Ref. [31]. (d) The ratio  $c/a$  vs.  $Ln$ . (e) The unit cell volume  $V$  vs.  $Ln$ . The dashed lines are guides to the eye.

15.6 K, and  $T_{N3} = 13.8$  K and  $TbAuAl_4Ge_2$  exhibits two magnetic phase transitions at  $T_{N1} = 13.9$  K and  $T_{N2} = 9.8$  K. All of these transitions are antiferromagnetic-like in low fields, but magnetic fields applied in the  $ab$  plane drive metamagnetic phase transitions into spin polarized states.

From these measurements, we construct  $T - H$  magnetic phase diagrams, where there are several regions with complex magnetic configurations. Heat capacity measurements additionally show that a substantial fraction of the magnetic entropy is found at temperatures above the ordered states, consistent with the presence of magnetic fluctuations (and crystal electric field effects for  $TbAuAl_4Ge_2$ ) [34–37]. Finally, the temperature dependent electrical resistivity for  $GdAuAl_4Ge_2$  exhibits a broad minimum that precedes the ordered state, providing evidence for possible magnetic frustration [38,39]. Taken together, these measurements reveal that although these compounds form with a relatively simple crystal structure, they nonetheless exhibit magnetic degeneracy that resembles what is seen for other centrosymmetric skyrmion lattices such as  $Gd_2PdSi_3$ . This invites further investigation to determine whether they are hosts for magnetically ordered states with multiple  $q$ -vectors or nontrivial magnetic topologies, where phenomena such as the topological Hall effect might be observed.

## 2. Experimental methods

$LnAuAl_4Ge_2$  ( $Ln = Y, Pr, Nd, Sm, Gd, Tb, Dy, Ho, Er,$  and  $Tm$ ) single crystals were grown using an aluminum molten metal flux, as previously reported [31]. Elements with purities  $> 99.9\%$  were combined in the molar ratio 1(RE):1(Au):10(Al):5(Ge) and loaded into 2-mL alumina Canfield crucibles [40]. The crucibles were sealed under vacuum in quartz tubes, heated to 1000 °C at a rate of 83 °C/h, kept at 1000 °C for 15 h, then cooled to 860 °C at a rate of 7 °C/h. The melt was then annealed at 860 °C for 48 h with the goal of improving sample quality and surfaces. In order to minimize thermal shock, this was followed by cooling down to 700 °C at a rate of 12 °C/h, after which excess flux was removed by centrifuging the tubes at 700 °C. Crystals are typically formed as three-dimensional clusters, where single crystals

with dimensions on the order of 2 mm and triangular facets associated with the  $ab$  plane could be isolated.

Room temperature powder X-ray diffraction (PXRD) measurements were performed using a Rigaku SmartLab SE X-ray diffractometer with a  $Cu K\alpha$  source. Crystal structure refinement analysis was performed using the Winprep software (Fig. S1, supplementary materials). The principal axes were identified using an Enraf-Nonius CAD-4 diffractometer, where the orientation of the full reciprocal lattice is obtained. EDAX measurements were also performed for the Gd and Tb compounds in order to verify the chemical composition. Magnetization  $M$  measurements were carried out at temperatures  $T = 1.8$ –300 K under applied magnetic fields of  $\mu_0 H = 0.5$ –9 T applied parallel ( $\parallel$ ) to the crystallographic  $c$  axis and the  $ab$  plane using a Quantum Design VSM Magnetic Property Measurement System. Specific heat  $C$  measurements were performed for temperatures  $T = 1.8$ –70 K in a Quantum Design Physical Properties Measurement Systems using a conventional thermal relaxation technique. DC electrical resistivity  $\rho$  measurements for temperatures  $T = 1.8$ –300 K were performed in a four-wire configuration for polished single crystal using the same system.

## 3. Results

### 3.1. $LnAuAl_4Ge_2$ X-ray diffraction

It was previously reported that  $CeAuAl_4Ge_2$  crystallizes in a well-ordered rhombohedral structure with space group  $R\bar{3}m$  [31,32] where the cerium ions are in the trivalent state. In Fig. 1 we present powder X-ray diffraction patterns for the other members of the  $LnAuAl_4Ge_2$  series ( $Ln = Y, Pr, Nd, Sm, Gd, Tb, Dy, Ho, Er,$  and  $Tm$ ), showing that the same structure persists across the lanthanide series (except Eu). Production of large phase pure specimens is challenging, as evidenced by the presence of extra peaks in the XRD pattern that do not belong to the  $LnAuAl_4Ge_2$  structure. For  $Ln = Pr$  and  $Nd$ , the impurity peaks are due to  $AuAl_2$  and  $LnAl_2Ge_2$ , but for  $Ln = Y, Dy, Ho, Er,$  and  $Tm$  only the  $LnAl_2Ge_2$  impurity is present. [41,42]. In the latter case, there is a close similarity between  $LnAl_2Ge_2$  and the  $LnAuAl_4Ge_2$  phases, which likely

**Table 1**

Summary of magnetic properties for GdAuAl<sub>4</sub>Ge<sub>2</sub> and TbAuAl<sub>4</sub>Ge<sub>2</sub> obtained from the magnetic susceptibility  $\chi(T)$ , the magnetization  $M(H)$ , and the heat capacity  $C(T)$ .  $\chi(T)$  was collected in a magnetic field  $\mu_0 H = 0.5$  T.  $C(T)$  and  $\rho(T)$  were collected in  $\mu_0 H = 0$  T.  $T_{N1}$ ,  $T_{N2}$ , and  $T_{N3}$  are the ordering temperatures,  $H_{C1}$ ,  $H_{C2}$ , and  $H_{C3}$  are critical fields at  $T = 1.8$  K,  $\theta$  and  $\mu_{\text{eff}}$  are the Curie-Weiss temperatures and the effective magnetic moments obtained from fits to  $\chi(T)$ , and  $M_{\text{sat}}$  is that saturation moment obtained from  $M(H)$ .

	$T_{N1}$ (K)	$T_{N2}$ (K)	$T_{N3}$ (K)	$H_{C1}$ (T)	$H_{C2}$ (T)	$H_{C3}$ (T)	$\theta$ (K)	$\mu_{\text{eff}}$ ( $\mu_B$ /F.U.)	$M_{\text{sat}}$ ( $\mu_B$ /F.U.)
Gd	17.8	15.6	13.8	1.9	–	–	2.3	7.93	–
Tb	13.9	9.8	–	1.3	1.9	2.7	18	9.89	8.31

relates to its tendency to appear in these crystals. We also find that the  $Ln = \text{Ce, Gd, Tb, and Sm}$  compound can be more easily obtained as phase-pure crystals. Rietveld refinements were performed for the entire series and the obtained lattice parameters ( $a$  and  $c$ ), the ratio ( $c/a$ ), and the unit cell volume ( $V$ ) are plotted in Fig. 1c–e, where their variation is consistent with a trivalent lanthanide contraction that isotropically compresses the unit cell. This behavior is expected since the radius of the lanthanide ions decreases with increasing atomic number, as long as the valence is fixed.

### 3.2. GdAuAl<sub>4</sub>Ge<sub>2</sub>

The temperature-dependent magnetic susceptibility  $\chi(T) = M/H$  for GdAuAl<sub>4</sub>Ge<sub>2</sub> is shown in Fig. 2. Fits to the data for  $H \parallel ab$  using the expression  $\chi = C/(T - \theta)$  yield the parameters  $\theta = 2.3$  K and  $\mu_{\text{eff}} = 7.93 \mu_B/\text{Gd}$  ( $\mu_{\text{eff}} = 7.94 \mu_B$  for Gd<sup>3+</sup>). It is noteworthy that there is a slight anisotropy between the curves for  $H \parallel ab$  and  $c$ . The reason for this is not clear, but similar behavior is seen in some other Gd-based materials and may relate to the anisotropic crystalline structure [43,44]. Anisotropic and field dependent magnetic ordering is seen at low temperatures (Fig. 2c,d). For  $\mu_0 H = 0.5$  T applied in the  $ab$ -plane, there are three distinct transitions at  $T_{N1} = 17.8$  K,  $T_{N2} = 15.6$  K, and  $T_{N3} = 13.8$  K which are defined from the derivative of the magnetic susceptibility  $\partial\chi/\partial T$  (panels e and f, Table 1). In the low field region, each transition decreases the magnitude of  $\chi$  (i.e., they are antiferromagnetic-like), and they are suppressed with increasing  $H$ . There are abrupt changes in these trends above  $\mu_0 H = 1.5$  T, where  $\chi(T)$  no longer strongly decreases at  $T_{N1}$  and instead tends to saturate or weakly decrease at low temperatures. This is consistent with the occurrence of field driven metamagnetic phase transitions where the spins abruptly become partially polarized. Within the partially spin polarized state,  $T_{N1}$  continues to be suppressed by field and there are additional features at  $T_{FM1}$  and  $T_{FM2}$  that suggest further weak spin reorientations. These transitions are seen as subtle features in  $\chi(T)$  and its temperature derivative (Fig.S2, supplementary materials), but future work is needed to fully clarify the spin states that are associated with them. It is also seen that for  $H \parallel c$ ,  $\chi(T)$  only clearly shows the transitions at  $T_{N1}$  and  $T_{N3}$ , which are gradually suppressed with  $H$ .

Isothermal magnetization  $M(H)$  measurements are shown in Fig. 3. For  $H \parallel c$  at  $T = 1.8$  K,  $M(H)$  increases linearly with applied field and does not saturate by 7 T. For  $H \parallel ab$  at  $T = 1.8$  K,  $M(H)$  initially exhibits a linear increase in the magnetization, then undergoes an abrupt and hysteretic increases at  $H_{C1} = 1.9$  T. Such behavior can be associated with a first order spin transition where the spins become partially polarized.  $M(H)$  subsequently increases linearly and does not saturate for  $\mu_0 H < 7$  T, where it reaches 57% of the expected value for Gd<sup>3+</sup> ( $M_{\text{sat}} = n g_J \mu_B J = 7 \mu_B/\text{Gd}$ ). This transition moves towards lower fields with increasing temperature, where it is seen at 10 K but is no longer observed at 15 K.

These results are used to construct the phase diagrams shown in Fig. 4a, where a rich family of ordered phases is seen for  $H \parallel ab$ . Starting from the paramagnetic state at low  $H$ , we find that the transition at  $T_{N1}$  weakly reduces  $\chi$  upon entering an antiferromagnetic-like region (wAFM1). This is rapidly replaced by another transition that further reduces  $\chi$  upon entering another antiferromagnetic-like region (wAFM2). Finally, there is a strong reduction in  $\chi$  when the system undergoes a first order phase transition into the spin reoriented

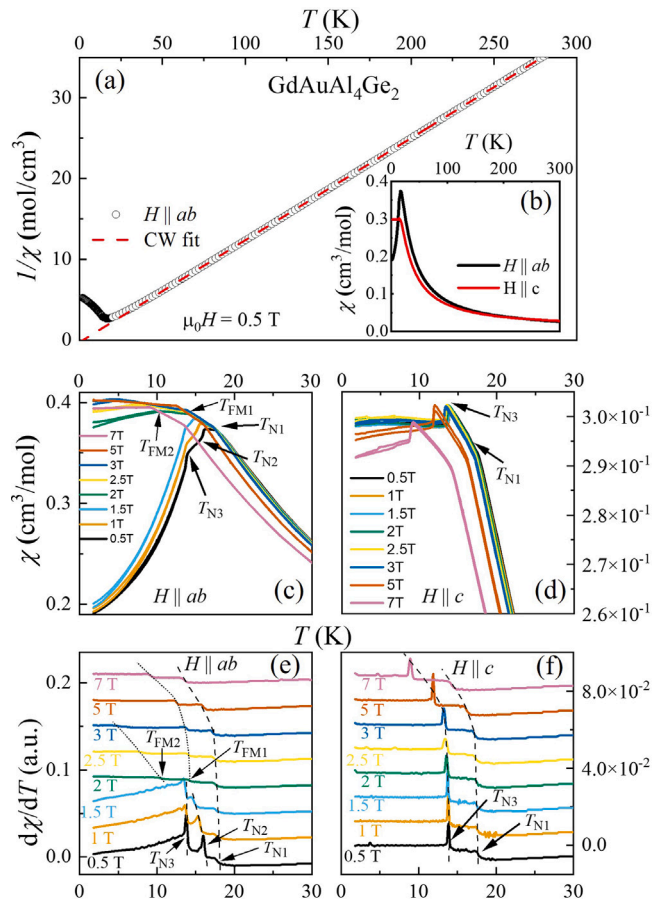
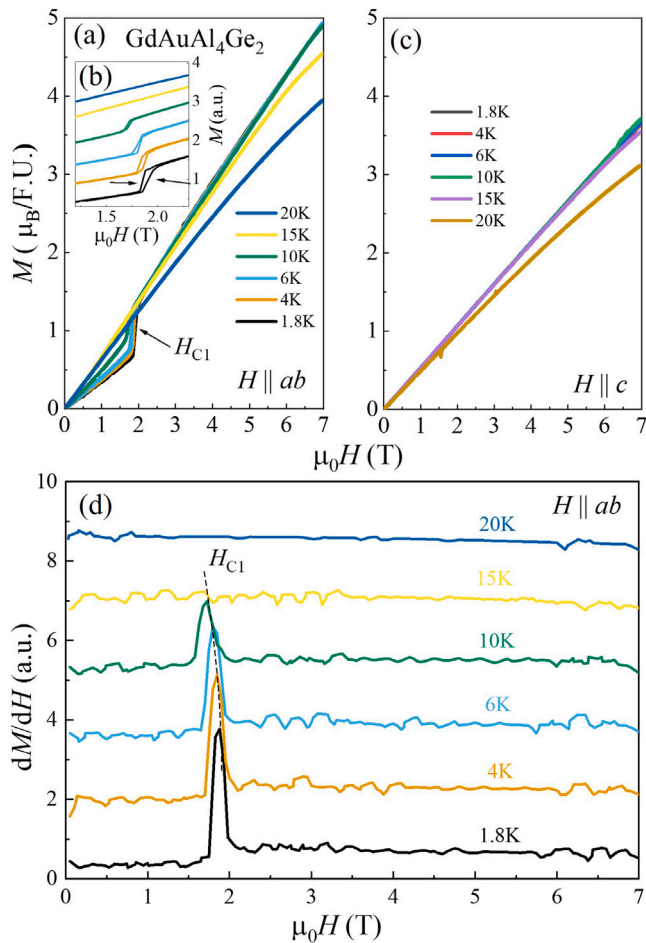


Fig. 2. (a) The inverse magnetic susceptibility  $\chi^{-1} = (M/H)^{-1}$  vs. temperature  $T$  for GdAuAl<sub>4</sub>Ge<sub>2</sub> collected in a magnetic field  $\mu_0 H = 0.5$  T applied parallel to  $ab$ -plane. The dotted line fits the data using the Curie-Weiss law, as described in the text. (b)  $\chi(T)$  for  $\mu_0 H = 0.5$  T applied both parallel (black line) to the  $ab$ -plane and  $c$ -axis (red line). (c, d)  $\chi(T)$  for  $1.8 \text{ K} < T < 30 \text{ K}$  emphasizing the region near the magnetic ordering temperatures  $T_{N1}$ ,  $T_{N2}$ ,  $T_{N3}$ ,  $T_{FM1}$ , and  $T_{FM2}$  which are defined in the text. (e, f) Derivatives of the magnetic susceptibilities with respect to temperature  $\frac{\partial\chi}{\partial T}$ . Data have been shifted vertically for clarity, and the dashed lines and short dot lines are guided to the eye.

ground state (SR). The rapid progression of phases, and the reductions in  $\chi$ , suggest that the phases are characterized by progressively more anti-aligned spin configurations, which may feature complicated wave vectors. Above 1.5 T there is an abrupt change in the ordered state behavior, where the transition into the wAFM state continues to appear as a weak reduction from the paramagnetic behavior, but the low field reductions in  $\chi$  are replaced by partially spin polarized states labeled FM1 and FM2. These boundaries are suppressed with increasing field, and are extrapolated to collapse towards zero temperature near 8–10 T. The low temperature boundary between SR and FM1 is clearly seen in the field dependent magnetization, where it appears as a hysteretic first order metamagnetic step. These results are contrasted with what is seen when fields are applied along the  $c$  axis (Fig. 4b), where the phase boundaries are gradually suppressed with  $H$ .



**Fig. 3.** (a) Isothermal magnetic field dependent magnetization  $M(H)$  for  $GdAuAl_4Ge_2$  with fields applied in the  $ab$  plane. (b) Zoom of the region near the metamagnetic phase transition at  $H_{C1}$ . Data are shifted vertically for clarity. (c)  $M(H)$  for fields along the  $c$ -axis. (d) The derivative of the magnetization  $\frac{\partial M}{\partial H}$  for  $H \parallel ab$  at various temperature. Data have been shifted vertically for clarity, and the dashed line is a guide to the eye.

Heat capacity divided by temperature  $C/T$  data are compared to those of the  $J = 0$  nonmagnetic analogue  $YAuAl_4Ge_2$  in Fig. 5a. As expected, there is close agreement between these curves at elevated temperatures, where phonons dominate the heat capacity. However, for  $T \lesssim 60$  K, the Gd curve begins to deviate from the Y behavior. In order to expose this trend, it is desirable to calculate the isolated magnetic contribution given by  $C_{mag}/T = (C_{Gd} - C_Y)/T$ . Earlier studies have shown that it may be necessary to renormalize the heat capacity of the nonmagnetic analogue to account for the impact of the differing Gd/Y masses on the phonon behavior. A method to do this is outlined in Ref. [45], where a renormalization ratio  $\rho_{ren} = \frac{\theta_D(GdAuAl_4Ge_2)}{\theta_D(YAuAl_4Ge_2)} = \left( \frac{1 * (M_Y)^{3/2} + 1 * (M_{Au})^{3/2} + 4 * (M_{Al})^{3/2} + 2 * (M_{Ge})^{3/2}}{1 * (M_{Gd})^{3/2} + 1 * (M_{Au})^{3/2} + 4 * (M_{Al})^{3/2} + 2 * (M_{Ge})^{3/2}} \right)^{1/3}$  is introduced. In this expression,  $M$  are the molar masses of the constituent atoms. Based on this, we calculate  $\rho_{ren} \approx 0.9384$ , which indicates that the Y heat capacity is a good approximation for the lattice component of the Gd heat capacity. From this analysis, we extract  $C_{mag}/T$  where a long and increasing tail precedes the ordered states. Consistent with  $\chi(T)$ , three distinct transitions are subsequently seen at  $T_{N1}$ ,  $T_{N2}$ , and  $T_{N3}$ . While the first two have typical second order  $\lambda$ -shape peaks, the feature at  $T_{N3}$  is sharp and hysteretic, which confirms that it is a first-order phase transition. Finally, we determine the magnetic contribution to the entropy  $S_{mag}(T)$  (Fig. 5c,d) by integrating  $C_{mag}/T$  for  $T > 1.8$  K.  $S_{mag}(T)$  reaches  $12.8 \text{ J mol}^{-1} \text{ K}^{-1}$  at  $T_{N1}$ , which is reduced from the full theoretical magnetic entropy given by  $S_{mag} = R \ln(2J + 1) = 17.3$

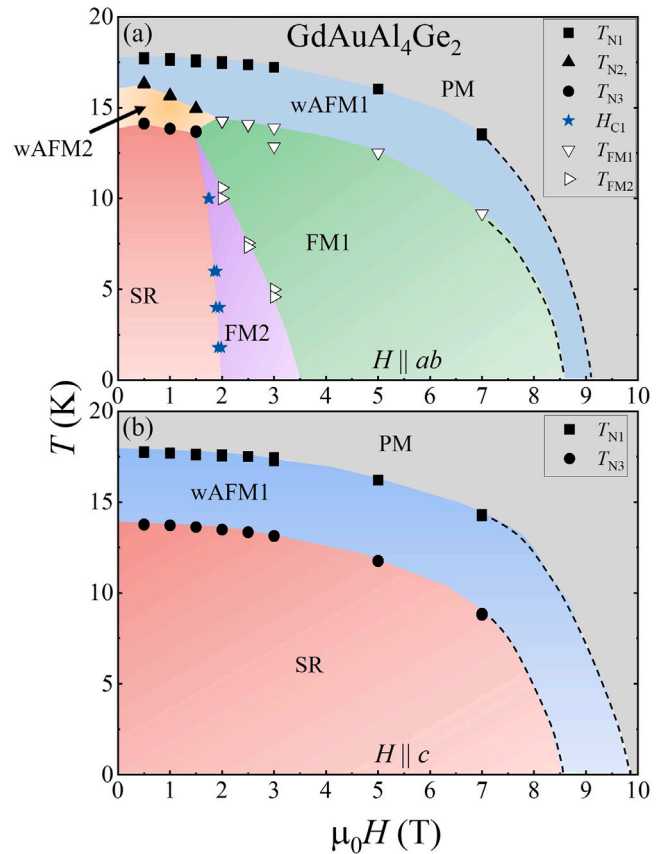


**Fig. 4.** Temperature  $T$  vs. magnetic field  $H$  phase diagram for  $GdAuAl_4Ge_2$  constructed from the magnetic susceptibility  $\chi(T)$  and isothermal magnetization  $M(H)$ . The zero field phase transitions agree with results from heat capacity  $C(T)$ , and electrical resistivity  $\rho(T)$  data, described below. The various regions wAFM1, wAFM2, SR, FM1, and FM2 are described in the text, where the phase boundaries separating wAFM1, wAFM2, and SR represent spin reorientations. Open symbols represent weak features that are only observed in  $\chi(T)$ .

$\text{J mol}^{-1} \text{ K}^{-1}$  ( $S = 7/2$ ,  $L = 0$ , and  $J = 7/2$ ). After this,  $S_{mag}$  continues to increase until it reaches a saturated value near  $16.4 \text{ J mol}^{-1} \text{ K}^{-1}$  for  $T \approx 40$  K. Given that crystal electric field splitting is not expected to influence the behavior of Gd, this suggests that the excess entropy above  $T_{N1}$  may originate from magnetic fluctuations of the Gd ions. However, we also point out that our analysis may not fully account for the entropy associated with the first order phase transition at  $T_{N3}$ .

Fig. 6 shows the temperature dependent electrical resistivity  $\rho(T)$ , with the electrical current applied in an arbitrary direction. Metallic behavior is observed from room temperature, where the phonon–electron term is dominant for  $50 < T < 300$  K. The magnetic ordering is preceded by a weak minimum that is centered near  $33.8$  K. This resembles what is seen for  $Gd_2PdSi_3$ , where the minimum in the resistivity is thought to be associated with an interplay between the RKKY interaction and magnetic frustration [38,39].  $T_{N1}$  and  $T_{N2}$  slightly reduce  $\rho$ , and there is a strong decrease at  $T_{N3}$ . This shows (i) that spin fluctuations above the ordered state enhance  $\rho$  and (ii) that the ordering removes of spin scattering of conduction electrons.

### 3.3. $TbAuAl_4Ge_2$

The temperature dependent magnetic susceptibility for  $TbAuAl_4Ge_2$  is shown in Fig. 7, where there is strong anisotropy that is associated with the non-zero angular momentum ( $L = 3$ ). The spins prefer to align in the  $ab$ -plane, and a Curie–Weiss temperature dependence for  $100 \text{ K} < T < 300 \text{ K}$  is observed. Fits to the data yield the parameters  $\theta =$

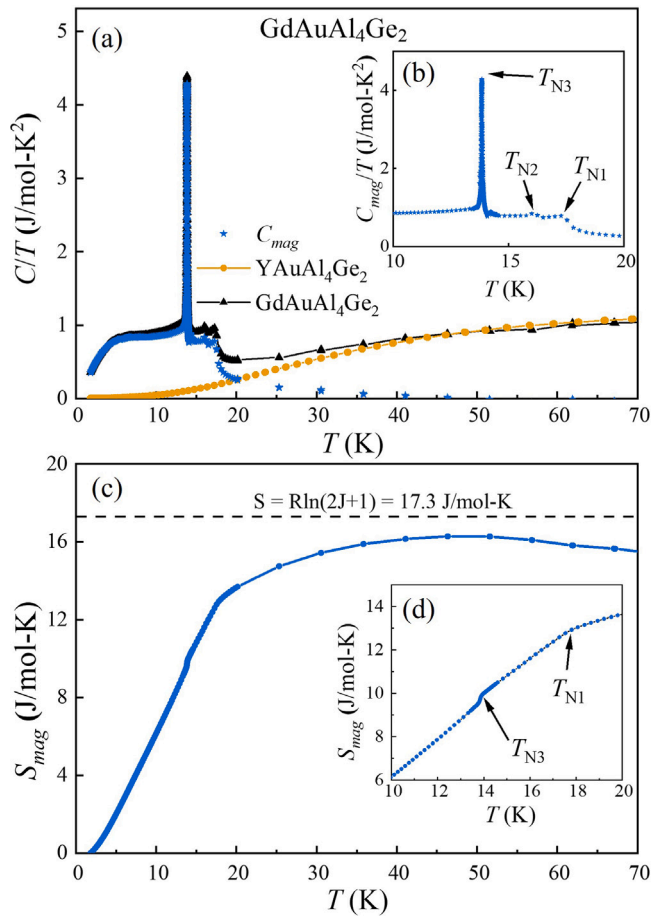


**Fig. 5.** (a) The heat capacity divided by temperature  $C/T$  vs.  $T$  for  $\text{GdAuAl}_4\text{Ge}_2$  and  $\text{YAuAl}_4\text{Ge}_2$ .  $C_{\text{mag}}$  is calculated as described in the text. (b) Zoom of  $C_{\text{mag}}/T$  near the transition temperatures. (c) Magnetic entropy  $S_{\text{mag}}$  vs.  $T$ , which is obtained from the heat capacity data as described in the text. The dotted line represents the calculated entropy for the full  $J = 7/2$  Hund's rule multiplet. (d) Zoom of  $S_{\text{mag}}$  in the region near the magnetic ordering.

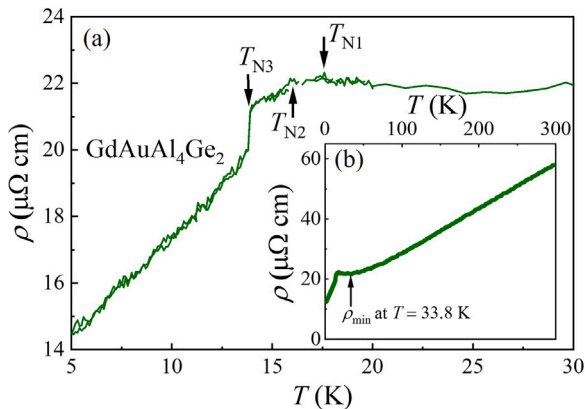


**Fig. 6.** Electrical resistivity  $\rho(T)$  at zero magnetic fields with the electrical current applied in an arbitrary direction for  $\text{GdAuAl}_4\text{Ge}_2$ . The main panel (a) shows the low temperature region near the phase transitions.  $T_{\text{N1}}$  and  $T_{\text{N2}}$  from  $\chi(T)$  are marked. The inset figure (b) shows the full temperature range between  $1.8 \text{ K} < T < 300 \text{ K}$ . Resistivity minimum at  $T = 33.8 \text{ K}$  is marked with an arrow.

$18.0 \text{ K}$  and  $\mu_{\text{eff}} = 9.89 \mu_{\text{B}}/\text{Tb}$  ( $\mu_{\text{eff}} = 9.72 \mu_{\text{B}}$  for  $\text{Tb}^{3+}$ ). For  $H \parallel c$ , the weak  $T$  dependence makes it difficult to perform a reliable Curie-Weiss fit. The ordered state behaviors are shown in Fig. 7c,d, where antiferromagnetic-like phase transitions at  $T_{\text{N1}} = 13.9 \text{ K}$  and  $T_{\text{N2}} = 9.8 \text{ K}$

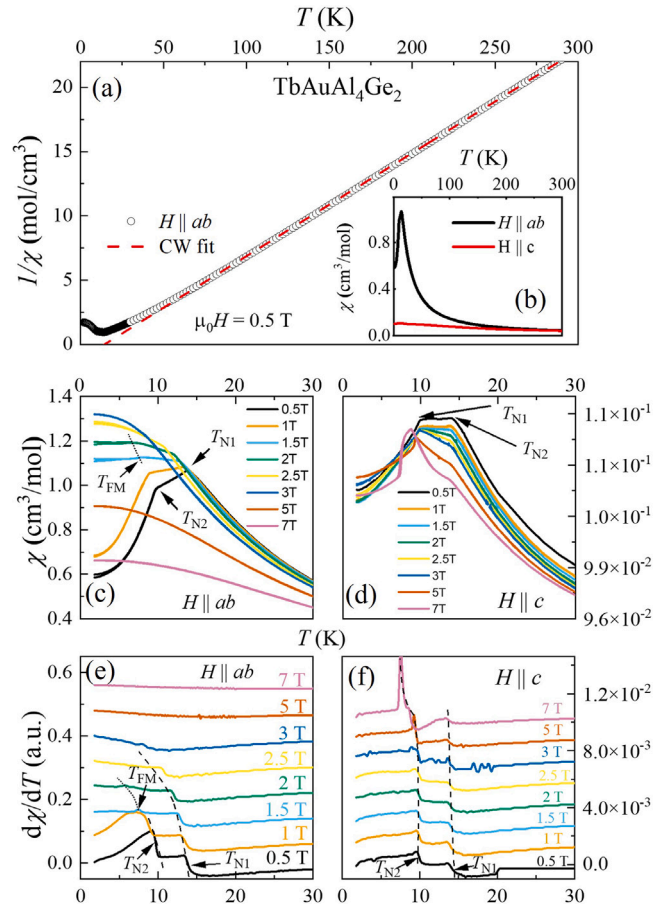


**Fig. 7.** (a) The inverse magnetic susceptibility  $\chi^{-1} = (M/H)^{-1}$  vs. temperature  $T$  for  $\text{TbAuAl}_4\text{Ge}_2$  collected in a magnetic field  $\mu_0 H = 0.5 \text{ T}$  applied parallel to  $ab$ -plane. The dotted line is a fit to the data using the Curie-Weiss law, as described in the text. (b)  $\chi(T)$  for  $\mu_0 H = 0.5 \text{ T}$  applied both parallel (black line) to the  $ab$ -plane and  $c$ -axis (red line). (c, d)  $\chi(T)$  for  $1.8 \text{ K} < T < 30 \text{ K}$  emphasizing the region near the magnetic ordering temperatures  $T_{\text{N1}}$ ,  $T_{\text{N2}}$ , and  $T_{\text{FM}}$  which are defined in the text. (e, f) Derivatives of the magnetic susceptibilities with respect to temperature  $\frac{\partial \chi}{\partial T}$ . Data have been shifted vertically for clarity, and the dashed lines and short dot lines are guided to the eye.

are seen for  $\mu_0 H = 0.5 \text{ T}$  applied in both directions. For  $H \parallel ab$ ,  $T_{\text{N1}}$  and  $T_{\text{N2}}$  are suppressed with increasing  $\mu_0 H$  up to  $1 \text{ T}$ , after which larger fields produce a field polarized state with a subphase that appears as a weak reduction of  $\chi(T)$  at  $T_{\text{FM}}$ . Fig. 7e,f shows  $\partial \chi / \partial T$ , where for  $H \parallel ab$  the transitions at  $T_{\text{N1}}$  and  $T_{\text{N2}}$  are seen as steps that are visible up to  $\mu_0 H = 1 \text{ T}$ . Above this,  $T_{\text{N1}}$  is suppressed with increasing  $H$  until it is no longer observed above  $3 \text{ T}$ . There is also weak feature within the field polarized state at  $T_{\text{FM}}$  that resembles what is seen for the Gd analogue. Further work is needed to clarify the spin orientation that is associated with it. For  $H \parallel c$  the features at  $T_{\text{N1}}$  and  $T_{\text{N2}}$  evolve in a more complicated way. While  $T_{\text{N1}}$  is nearly field independent,  $T_{\text{N2}}$  evolves from being a second-order-like reduction in  $\chi$  towards a much sharper decrease, which resembles what is seen for the Gd analogue in low fields.

Isothermal magnetization  $M(H)$  measurements are shown in Fig. 8. For  $H \parallel ab$  at  $T = 1.8 \text{ K}$ , the magnetization initially increases linearly and undergoes an abrupt and hysteretic increase at  $H_{\text{C1}} = 1.3 \text{ T}$ . This is followed by several additional transitions at  $H_{\text{C2}} = 1.9 \text{ T}$  and  $H_{\text{C3}} = 2.7 \text{ T}$ , which are revealed in the derivative of the magnetization  $\partial M / \partial H$  (Fig. 8c, Table 1). The magnetization finally reaches a value of  $8.31 \mu_{\text{B}}/\text{F.U}$  at  $7 \text{ T}$ , which is 92% of the expected saturation value ( $M_{\text{sat}} = 9 \mu_{\text{B}}/\text{Tb}$ ). Increasing temperature causes the transitions to broaden and while  $H_{\text{C1}}$  is gradually suppressed,  $H_{\text{C2}}$  and  $H_{\text{C3}}$  move towards larger

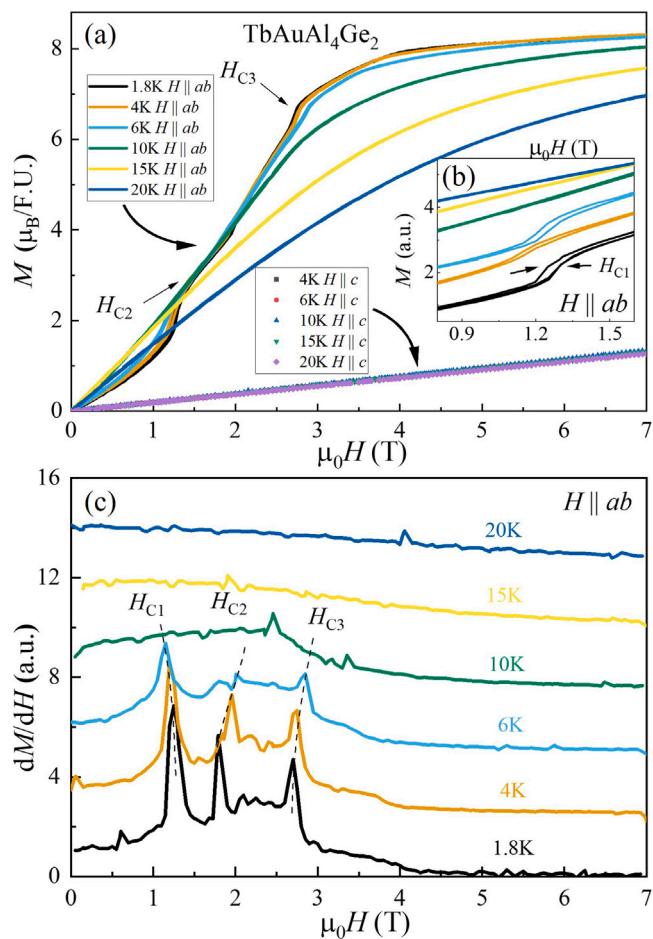


Fig. 8. (a) Isothermal magnetic field dependent magnetization  $M(H)$  for  $\text{TbAuAl}_4\text{Ge}_2$  with fields applied in the  $ab$  plane and along the  $c$ -axis. (b) Zoom of  $M(H)$  near the metamagnetic phase transitions at  $H_{C1}$ ,  $H_{C2}$ , and  $H_{C3}$ . Data are shifted vertically for clarity. (c) The derivative of the magnetization  $\frac{\partial M}{\partial H}$  for  $H \parallel ab$  at various temperature. The curves have been shifted vertically and the dashed lines are guided to the eye.

values. In contrast to this,  $M(H)$  for  $H \parallel c$  increases linearly with  $H$  and shows no evidence for any transitions.

The resulting phase diagrams are shown in Fig. 9, where there are noteworthy similarities to what is seen for  $\text{GdAuAl}_4\text{Ge}_2$ . For  $H \parallel ab$  and at low  $H$ , the system undergoes a second order transition into a state that reduces  $\chi$  below the extrapolated paramagnetic curve (wAFM1). This is rapidly followed by another second order transition that further reduces  $\chi$  (SR). Again, this suggests that each of these transitions represents progressively more antialigned spin configurations with complicated wave vectors. Above  $\mu_0 H \approx 1.5$  T there is an abrupt change in the ordered state behavior, where the transition into the wAFM state continues to appear as a weak reduction from the paramagnetic behavior, but the low field reductions in  $\chi$  are replaced by spin polarized states labeled FM1 and FM2. These boundaries are suppressed with increasing field, but unlike what is seen for  $\text{GdAuAl}_4\text{Ge}_2$ , are sharply truncated and collapse towards zero temperature near 2.5–3 T. The low temperature boundaries between SR, FM1, and FM2 are clearly seen in the field dependent magnetization, where the boundary between SR and FM1 appears as a hysteretic first order metamagnetic step, and the subsequent boundaries are broader increases in  $M$ . The  $T-H$  phase diagram is much simpler when fields are applied along the  $c$  axis (Fig. 9b), where the phase boundaries are gradually suppressed with  $H$ .

The heat capacity divided by temperature  $C/T$  data are compared to those for  $\text{YAuAl}_4\text{Ge}_2$  in Fig. 10. As for the Gd analogue, at elevated

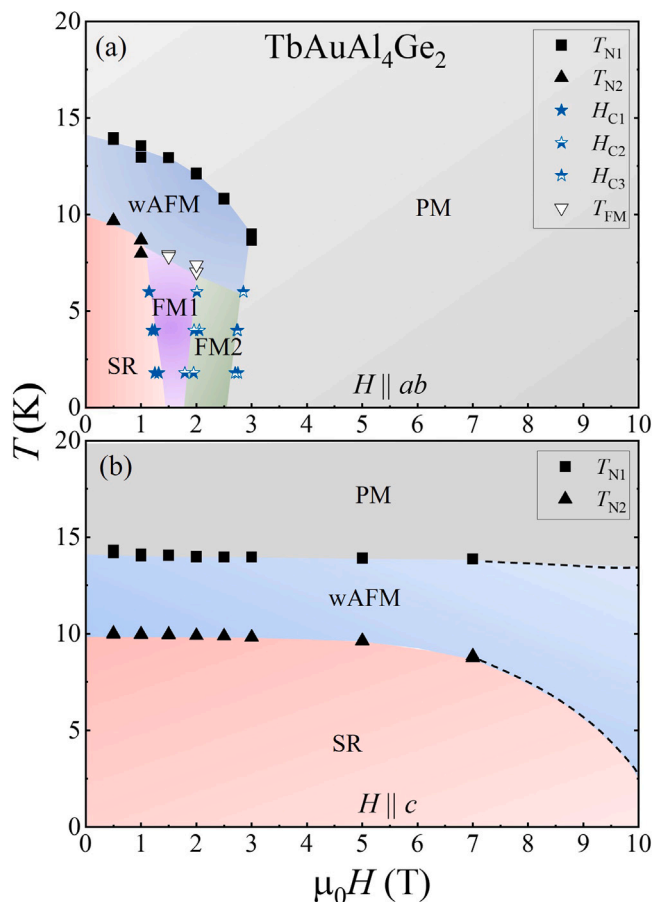
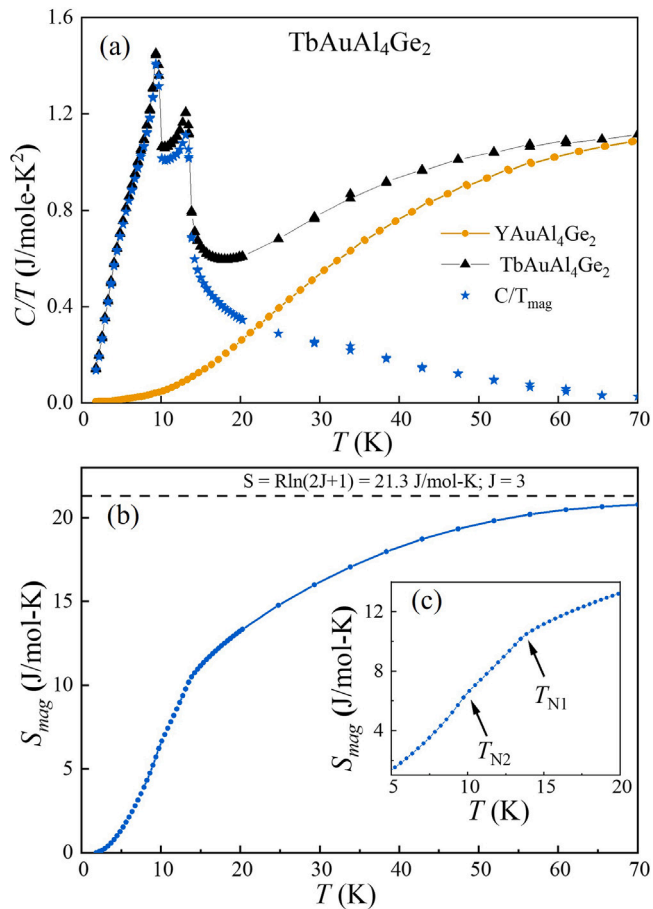


Fig. 9. Temperature  $T$  vs. magnetic field  $H$  phase diagram for  $\text{TbAuAl}_4\text{Ge}_2$  constructed from the magnetic susceptibility  $\chi(T)$  and isothermal magnetization  $M(H)$ . The zero field phase transition agrees with results from heat capacity  $C(T)$ , and electrical resistivity  $\rho(T)$  data, described below. The various regions wAFM1, wAFM2, SR, FM1, and FM2 are described in the text.

temperatures there is close agreement between the data sets but for  $T \lesssim 70$  K, the data deviate from what is seen for the Y compound. By applying the analysis described above for the Gd analogue, we find  $\rho_{\text{ren}} = 0.937$  and conclude that the Y heat capacity again provides a reasonable estimate for the phonon contribution. From this, we find that the isolated magnetic contribution  $C_{\text{mag}}/T = (C_{\text{Tb}} - C_{\text{Y}})/T$  exhibits a long and increasing tail precedes the ordered states and that ordering is seen at  $T_{N1} = 13.9$  K,  $T_{N2} = 9.8$  K as second-order peaks. The magnetic entropy  $S_{\text{mag}}(T)$  is shown in Fig. 10c, where  $S_{\text{mag}}(T)$  reaches  $13.9$  J  $\text{mol}^{-1} \text{K}^{-1}$  at  $T_{N1}$ . Again this value is reduced from the expected value  $S_{\text{mag}} = R \ln(2J + 1) = 21.3$  J  $\text{mol}^{-1} \text{K}^{-1}$  ( $S = 3$ ,  $L = 3$ , and  $J = 6$ ). After this it continues to increase until reaching a saturation value of  $20.7$  J  $\text{mol}^{-1}$  near  $T \approx 70$  K. This provides evidence that (i) the crystal electric field split levels are fully populated around this temperature and (ii) magnetic fluctuations may extend well above the ordered state, although the influences of these factors are not distinguishable.

Fig. 11 shows the temperature dependence of the electrical resistivity  $\rho(T)$  for  $\text{TbAuAl}_4\text{Ge}_2$  with the electrical current applied in an arbitrary direction. Metallic behavior is observed from room temperature, where the phonon–electron term is dominant for  $50 < T < 300$  K. It is noteworthy that the minimum that is seen for the Gd analogue does not appear here. Finally, the rapid decrease in  $\rho(T)$  coincides with the onset of the magnetic ordering at  $T_{N1}$  and indicates the significant removal of spin scattering of conduction electrons.



**Fig. 10.** (a) The heat capacity divided by temperature  $C/T$  vs.  $T$  for  $\text{TbAuAl}_4\text{Ge}_2$  and  $\text{YAuAl}_4\text{Ge}_2$ .  $C_{\text{mag}}/T$  is calculated as described in the text. (b) Magnetic entropy  $S_{\text{mag}}$  vs.  $T$ , which is obtained from the heat capacity data as described in the text. The dotted line represents the calculated entropy for the full  $J = 6$  Hund's rule multiplet. (c) Zoom of  $S_{\text{mag}}$  in the region near the magnetic ordering temperatures.

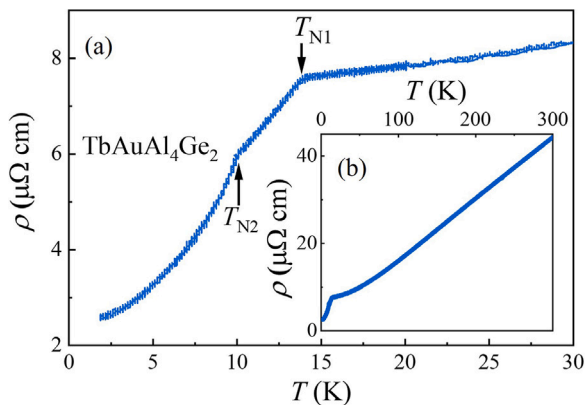


**Fig. 11.** Electrical resistivity  $\rho(T)$  at zero magnetic field with the electrical current applied in an arbitrary direction for  $\text{TbAuAl}_4\text{Ge}_2$ . The main panel shows the low temperature region near the phase transitions and the inset shows the full temperature range between  $1.8$  K <  $T$  <  $300$  K.

#### 4. Discussion

Taken together, these measurements show that both  $\text{GdAuAl}_4\text{Ge}_2$  and  $\text{TbAuAl}_4\text{Ge}_2$  exhibit complex magnetic phenomena with noteworthy similarities. Evidence for this includes (i) magnetic entropy that extends to temperatures well above the ordered states, (ii) a sharp drop

of resistivity as the magnetic order sets in, and (iii) the occurrence of multiple magnetically ordered states that are delicately tuned by magnetic fields. These features are shared by other magnetically frustrated materials that have nontrivial spin textures (e.g.,  $\text{Gd}_2\text{PdSi}_3$ ,  $\text{GdRu}_2\text{Si}_2$ , and  $\text{Gd}_3\text{Ru}_4\text{Al}_{12}$  [15–19]) and are currently motivating investigations of a variety of related materials (e.g.,  $Ln_2\text{RhSi}_3$   $Ln = \text{Gd}, \text{Tb}, \text{Dy}$  [39]). However, it is also well known that Gd and Tb based metals exhibit a wide variety of complex magnetic states with no obvious connection to skyrmion states [35,46]. Based on this, we propose that further studies that target the magnetic structure such as neutron scattering, Lorentz tunneling electron microscopy, and magnetic force microscopy will be of interest to clarify the behavior of the spins in these compounds. Also needed are efforts to investigate whether these compounds exhibit novel electrical transport properties such as a topological Hall effect. Moreover, since a first-order phase transition is seen in the  $\text{GdAuAl}_4\text{Ge}_2$  compound, it will be of interest to perform magnetization measurements under field-cooling conditions to look for novel thermomagnetic history effects [47,48].

Irrespective of whether any of these states exhibit nontrivial electronic behaviors such as the topological Hall effect, it will also be of interest to understand the various magnetically ordered phases that are present, the factors that drive differences or similarities between the Gd and Tb examples, and their interactions with other degrees of freedom. For example, it is currently unclear why the Gd case exhibits a cascade of transitions between the wAFM1, wAFM2, and SR states, along with a first order phase transition, while the Tb example does not. We speculate that this relates to differences in the magnetic interactions that are associated with the isotropic pure spin Gd ions and the anisotropic Tb ions, but more work is needed to verify this. It is also noteworthy that while  $\text{GdAuAl}_4\text{Ge}_2$  exhibits a resistivity minimum that precedes the ordering,  $\text{TbAuAl}_4\text{Ge}_2$  does not. This implies that variation of the lanthanide ions will likely be useful to optimize both magnetic frustration and the conditions for the formation of a possible skyrmion lattice.

#### 5. Conclusions

In summary, we have produced the series of compounds  $Ln\text{AuAl}_4\text{Ge}_2$  ( $Ln = \text{Y}, \text{Pr}, \text{Nd}, \text{Sm}, \text{Gd}, \text{Tb}, \text{Dy}, \text{Ho}, \text{Er}, \text{and Tm}$ ) and have focused on the bulk magnetic properties of the Gd and Tb variants. Temperature and magnetic field dependent magnetization, heat capacity, and electrical resistivity measurements show that both of these compounds exhibit several magnetically ordered states at low temperatures, with evidence for magnetic fluctuations extending into the paramagnetic temperature region. Applied magnetic fields produce several distinct magnetically ordered regions, where there are many similarities between the two compounds. This is surprising given their different orbital quantum numbers and suggests that the features of the crystalline lattice or the Fermi surface topography are dominant factors in determining the ground state behavior. Thus, the family of materials  $Ln\text{AuAl}_2\text{Ge}_2$  emerges as a reservoir for novel metallic magnetism and invites investigations into them to search for nontrivial spin structures and novel electronic behavior such as the topological Hall effect.

#### CRedit authorship contribution statement

**Keke Feng:** Data curation, Formal analysis, Investigation, Validation, Visualization, Writing – original draft, Writing – review & editing. **Ian Andreas Leahy:** Data curation, Formal analysis, Investigation, Validation, Visualization, Writing – original draft, Writing – review & editing. **Olatunde Oladehin:** Investigation, Validation. **Kaya Wei:** Investigation, Validation. **Minhyea Lee:** Data curation, Formal analysis, Investigation, Validation, Visualization, Writing – original draft, Writing – review & editing. **Ryan Baumbach:** Conceptualization, Data curation, Formal analysis, Funding acquisition, Investigation, Methodology, Project administration, Resources, Supervision, Validation, Visualization, Writing – original draft, Writing – review & editing.

## Declaration of competing interest

The authors declare that they have no known competing financial interests or personal relationships that could have appeared to influence the work reported in this paper.

## Data availability

Data will be made available on request.

## Acknowledgments

RB, KF, and OO were supported by the National Science Foundation, United States of America through NSF DMR-1904361. Work at the University of Colorado Boulder was supported by Award No. DE-SC0021377 of the U.S. Department of Energy, Basic Energy Sciences, Materials Sciences, and Engineering Division. The National High Magnetic Field Laboratory is supported by the National Science Foundation, United States of America through NSF DMR-1644779 and the State of Florida, United States of America.

## Appendix A. Supplementary data

Supplementary material related to this article can be found online at <https://doi.org/10.1016/j.jmmm.2022.170006>.

## References

- [1] K.A. Gschneidner, L. Eyring, Handbook on the Physics and Chemistry, Volume 1, Metals North-Holland Publishing Company, New York, 1979.
- [2] K.A. Gschneidner, L. Eyring, Handbook on the Physics and Chemistry, Volume 2, Alloys and Intermetallics North-Holland Publishing Company, New York, 1979.
- [3] M. Sagawa, S. Fujimura, H. Yamamoto, Y. Matsuura, K. Hiraga, Permanent magnet materials based on the rare earth-iron-boron tetragonal compounds, *IEEE Trans. Magn.* 20 (1984) 1584.
- [4] K. Strnat, G. Hoffer, J. Olson, W. Ostertag, A Family of New Cobalt-Base Permanent Magnet Materials, *J. Appl. Phys.* 38 (1967) 1001.
- [5] G.R. Stewart, Heavy Fermion Systems, *Rev. Modern Phys.* 56 (1984) 755.
- [6] J.A. Mydosh, P.M. Oppeneer, P.S. Riseborough, Hidden Order and Beyond: an Experimental-Theoretical Overview of the Multifaceted Behavior of URu<sub>2</sub>Si<sub>2</sub>, *J. Phys. Condens. Matter* 32 (January) (2020) 143002.
- [7] H.S. Jeevan, C. Geibel, Z. Hossain, Quasiquartet Crystal-Electric-Field Ground State with Possible Quadrupolar Ordering in the Tetragonal Compound YbRu<sub>2</sub>Ge<sub>2</sub>, *Phys. Rev. B* 73 (January) (2006) 20407.
- [8] C. Pfleiderer, Superconducting Phases of *f*-electron Compounds, *Rev. Modern Phys.* 81 (November) (2009) 1551–1624.
- [9] M. Dzero, K. Sun, V. Galitski, P. Coleman, Topological Kondo Insulators, *Phys. Rev. Lett.* 104 (March) (2010) 106408.
- [10] M.A. Ruderman, C. Kittel, Indirect Exchange Coupling of Nuclear Magnetic Moments by Conduction Electrons, *Phys. Rev.* 96 (October) (1954) 99–102.
- [11] T. Kasuya, A Theory of Metallic Ferro- and Antiferromagnetism on Zener's Model, *Progr. Theoret. Phys.* 16 (July) (1956) 45–47.
- [12] K. Yosida, Magnetic Properties of Cu-Mn Alloys, *Phys. Rev.* 106 (June) (1957) 893–898.
- [13] D.J. Newman, Theory of lanthanide crystal fields, *Adv. Phys.* 20 (1971) 197.
- [14] J. Kondo, Resistance Minimum in Dilute Magnetic Alloys, *Progr. Theoret. Phys.* 32 (July) (1964) 37–49.
- [15] A.O. Leonov, M. Mostovoy, Multiply periodic states and isolated skyrmions in an anisotropic frustrated magnet, *Nature Commun.* 6 (2015) 8275.
- [16] S.Z. Lin, C.D. Batista, Face Centered Cubic and Hexagonal Close Packed Skyrmion Crystals in Centrosymmetric Magnets, *Phys. Rev. Lett.* 120 (2018) 077202.
- [17] M. Hirschberger, T. Nakajima, S. Gao, L. Peng, A. Kikkawa, T. Kurumaji, M. Kriener, Y. Yamasaki, H. Sagayama, H. Nakao, K. Ohishi, K. Kakurai, Y. Taguchi, X. Yu, T. h. Arima, Y. Tokura, Skyrmion phase and competing magnetic orders on a breathing kagomé lattice, *Nature Commun.* 10 (2019) 5831.
- [18] N.D. Khanh, T. Nakajima, Y. Tokura, S. Seki, Nanometric square skyrmion lattice in a centrosymmetric tetragonal magnet, *Nature Nanotechnol.* 15 (2020) 444.
- [19] T. Kurumaji, T. Nakajima, M. Hirschberger, A. Kikkawa, Y. Yamasaki, H. Sagayama, H. Nakao, Y. Taguchi, T. hisa Arima, Y. Tokura, Skyrmion lattice with a giant topological Hall effect in a frustrated triangular-lattice magnet, *Science* 365 (2019) 914.
- [20] S.S. Sunku, T. Kong, T. Ito, P.C. Canfield, B.S. Shastry, P. Sengupta, C. Panagopoulos, Hysteretic magnetoresistance and unconventional anomalous Hall effect in the frustrated magnet TmB<sub>4</sub>, *Phys. Rev. B* 93 (2016) 174408.
- [21] S. Mühlbauer, B. Binz, F. Jonietz, C. Pfleiderer, A. Rosch, A. Neubauer, R. Georgii, P. Böni, Skyrmion Lattice in a Chiral Magnet, *Science* 323 (2009) 915.
- [22] X. Z.Yu, Y. Onose, N. Kanazawa, J.H. Han, Y. Tokura, Real-space observation of a two-dimensional skyrmion crystal, *Nature* 465 (2010) 901.
- [23] H.M. Guo, M. Franz, Topological insulator on the kagome lattice, *Phys. Rev. B* 80 (2009) 113102.
- [24] M. Ezawa, Higher-Order Topological Insulators and Semimetals on the Breathing Kagome and Pyrochlore Lattices, *Phys. Rev. Lett.* 120 (2018) 026801.
- [25] W. Selke, The ANNNI model — Theoretical analysis and experimental application, *Phys. Rep.* 170 (1988) 213.
- [26] J. Rossat-Mignod, P. Burtel, J. Villain, H. Bartholin, W. Tcheng-Si, D. Florence, O. Vogt, Phase diagram and magnetic structures of CeSb, *Phys. Rev. B* 16 (1977) 440.
- [27] K.W. Chen, Y. Lai, Y.C. Chiu, S. Steven, T. Besara, D. Graf, T. Siegrist, T.E. Albrecht-Schmitt, L. Balicas, R.E. Baumbach, Possible devil's staircase in the Kondo lattice CeSbSe, *Phys. Rev. B* 96 (2017) 014421.
- [28] R. Feile, M. Loewenhaupt, J.K. Kjems, H.E. Hoenig, Influence of Superconductivity on Crystal Electric Field Transitions in La<sub>1-x</sub>Tb<sub>x</sub>Al<sub>3</sub>, *Phys. Rev. Lett.* 47 (1981) 610.
- [29] L.S. Silva, S.G. Mercena, D.J. Garcia, E.M. Bittar, C.B.R. Jesus, P.G. Pagliuso, R. Lora Serrano, C.T. Meneses, J.G.S. Duque, Crystal field effects in the intermetallic RNi<sub>3</sub>Ga<sub>3</sub> (R = Tb, Dy, Ho, and Er) compounds, *Phys. Rev. B* 95 (2017) 134434.
- [30] S. Ramakrishnan, N.G. Patil, A.D. Chinchure, V.R. Marathe, Magnetism and crystal-field effects in the R<sub>2</sub>Rb<sub>3</sub>Si<sub>2</sub> (R = La, Ce, Pr, Nd, Tb, Gd, Dy, Er, Ho, and Tm) system, *Phys. Rev. B* 64 (2001) 064514.
- [31] X. Wu, M. G.Kanatzidis, REAuAl<sub>3</sub>Ge<sub>2</sub> and REAuAl<sub>3</sub>(Au<sub>2</sub>Ge<sub>1-x</sub>)<sub>2</sub> (RE=rare earth element): Quaternary intermetallics grown in liquid aluminum, *J. Solid State Chem.* 178 (2005) 3233.
- [32] S. Zhang, N. Aryal, K. Huang, K.W. Chen, Y. Lai, D. Graf, T. Besara, T. Siegrist, E. Manousakis, R.E. Baumbach, Electronic structure and magnetism in the layered triangular lattice compound CeAuAl<sub>3</sub>Ge<sub>2</sub>, *Phys. Rev. Mater.* 1 (2017) 044404.
- [33] S.R. Saha, H. Sugawara, T.D. Matsuda, H. Sato, R. Mallik, E.V. Sampathkumaran, Magnetic anisotropy, first-order-like metamagnetic transitions, and large negative magnetoresistance in single-crystal Gd<sub>2</sub>PdSi<sub>3</sub>, *Phys. Rev. B* 60 (1999) 12162.
- [34] P. Kumar, K.G. Suresh, A.K. Nigam, Magnetism, heat capacity, magnetocaloric effect and magneto-transport in R<sub>2</sub>Al (R = Nd, Gd, Tb) compounds, *J. Phys. D: Appl. Phys.* 41 (2008) 105007.
- [35] M. Bouvier, P. Lethuillier, D. Schmitt, Specific heat in some gadolinium compounds. I. Experimental, *Phys. Rev. B* 43 (1991) 13137.
- [36] R. Mallik, E.V. Sampathkumaran, M. Strecker, G. Wortmann, Observation of a minimum in the temperature-dependent electrical resistance above the magnetic-ordering temperature in Gd<sub>2</sub>PdSi<sub>3</sub>, *Europhys. Lett.* (EPL) 41 (1998) 315.
- [37] S. Nakamura, N. Kabeya, M. Kobayashi, K. Araki, K. Katoh, A. Ochiai, Spin trimer formation in the metallic compound Gd<sub>3</sub>Ru<sub>4</sub>Al<sub>12</sub> with a distorted kagome lattice structure, *Phys. Rev. B* 98 (2018) 054410.
- [38] Zhenhao Wang, Kipton Barros, Gia-Wei Chern, Dmitrii L. Maslov, Cristian D. Batista, Resistivity Minimum in Highly Frustrated Itinerant Magnets, *Phys. Rev. Lett.* 117 (2016) 206601.
- [39] R. Kumar, K.K. Iyer, P.L. Paulose, E.V. Sampathkumaran, Magnetic and transport anomalies in R<sub>2</sub>RhSi<sub>3</sub> (R = Gd, Tb, and Dy) resembling those of the exotic magnetic material Gd<sub>2</sub>PdSi<sub>3</sub>, *Phys. Rev. B* 101 (2020) 144440.
- [40] P.C. Canfield, T. Kong, U.S. Kaluarachchi, N.H. Jo, Use of frit-disc crucibles for routine and exploratory solution growth of single crystalline samples, *Phil. Mag.* 96 (2016) 84.
- [41] C. Kranenberg, D. Johrendt, A. Mewis, The stability range of the CaAl<sub>2</sub>Si<sub>2</sub>-type structure in case of LnAl<sub>2</sub>Ge<sub>2</sub> compounds, *Solid State Sci.* 4 (2002) 261.
- [42] P. Qin, Y. Chen, J. He, W. He, L. Nong, L. Zeng, Investigation on structural and thermal expansion properties of Al<sub>2</sub>ErGe<sub>2</sub>, *Mater. Chem. Phys.* 109 (2008) 515.
- [43] D. Betancourth, J.I. Facio, P. Pedrazzini, C.B.R. Jesus, P.G. Pagliuso, V. Vil-dosola, Pablo S. Cornaglia, D.J. Garcia, V.F. Correa, Low-temperature magnetic properties of GdCoIn<sub>5</sub>, *J. Magn. Magn. Mater.* 374 (2015) 744–747.
- [44] P.G. Pagliuso, J.D. Thompson, M.F. Hundley, J.L. Sarrao, Z. Fisk, Crystal structure and low-temperature magnetic properties of R<sub>m</sub>MIn<sub>3m+2</sub> compounds (M=Rh or Ir; m=1, 2; R=Sm or Gd), *Phys. Rev. B* 63 (2001) 054426.
- [45] M. Bouvier, P. Lethuillier, D. Schmitt, Specific heat in some gadolinium compounds. I. Experimental, *Phys. Rev. B* 43 (1991) 13137–13144.
- [46] K. A.Gschneidner, L. Eyring, Handbook on the Physics and Chemistry of Rare Earths, Volume 1, Metals North-Holland Publishing Company, Amsterdam, 1982.
- [47] M.A. Manekar, S. Chaudhary, M.K. Chattopadhyay, K.J. Singh, S.B. Roy, Chaddah. P, First-order transition from antiferromagnetism to ferromagnetism in Ce(Fe<sub>0.96</sub>Al<sub>0.04</sub>)<sub>2</sub>, *Phys. Rev. B* 64 (2001) 104416.
- [48] V. Siruguri, P.D. Babu, S.D. Kaushik, Aniruddha Biswas, S.K. Sarkar, Madangopal Krishnan, P. Chaddah, Neutron diffraction evidence for kinetic arrest of first order magneto-structural phase transitions in some functional magnetic materials, *J. Phys.: Condens. Matter* 25 (2013) 496011.